Electronic Supplementary Information

Modulated Growth of High-Quality CsPbI$_3$ Perovskite Film by Molybdenum Modified SnO$_2$ Layer for Highly Efficient Solar Cells

Xiu Gong,[*a] Ting Wang,[a] Guilin Yin,[a] Qiong Peng,[a] Yanli Chen,[a] Xu Wang,[b] Xiaosi Qi,[*a] Yurong Jiang,[c] Zonghao Liu,[d] Yan Shen,[d] Mingkui Wang[*d]

[a]College of Physics, & Guizhou Province Key Laboratory for Photoelectrics Technology and Application, Guizhou University, Guiyang 550025, China

[b]College of Big Data and Information Engineering, Guizhou University, Guiyang 550025, China

[c]Henan Key Laboratory of Photovoltaic Materials, Henan Normal University, Xinxiang 453007, China

[d]Wuhan National Laboratory for Optoelectronics, School of Optical and Electronic Information, Huazhong University of Science and Technology, Wuhan, Hubei 430074, China

*Corresponding author.

E-mail: xgong@gzu.edu.cn; xsqi@gzu.edu.cn; mingkui.wang@mail.hust.eud.cn;

Materials

All chemicals used in the synthesis of Mo-doped SnO_2 nanoparticles were purchased from Aladdin without further purification. All chemicals and reagents used in the study of perovskites were purchased from Sigma-Aldrich without further purification.

Synthesis of Mo-doped SnO_2 Nanoparticles

Mo-doped SnO_2 nanoparticles with different doping levels were prepared according to a modified method.[1,2] $Na_2MoO_4 \cdot 2H_2O$ and $SnCl_4 \cdot 5H_2O$ (variable Mo doping concentrations at 0, 0.3, 0.5, 0.7, and 1 at.%) were dispersed in DI water by ultrasound, followed by dropwise addition of urea as a stabilizing agent to well control the hydrolysis reaction. Then the uniform solution was transferred to an autoclave and kept at 200°C for 24 h. After cooling to room temperature, the resulting white cloudy products were centrifuged, washed with DI water and ethanol by ultrasonication to remove the residual Cl^-, Na^+. This washing process was repeated at least three times. The white cloudy dried gel precipitates were finally dispersed again in ethanol at a concentration of 3-5 mg mL^{-1} for use to form compact films.

Device Characterization

X-ray photoelectron spectroscopy (XPS) was used to study the elemental composition of the pure and Mo-doped SnO_2. Ultraviolet photoelectron spectroscopy (UPS) measurements were performed to define the change of energy levels by a Kratos AXIS Ultra-DLD ultra-high-vacuum photoemission spectroscopy system with an Al Kα radiation source. The surface morphology for ETLs and perovskite films were characterized with a field-emission scanning elect` (FE-SEM). Tapping mode atomic force microscopy (AFM) was performed using a Veeco multimode instrument to identify surface roughness changes of the pure and Mo-doped SnO_2. TEM and HRTEM analysis were carried out on a FEIOSIRIS microscope. The X-ray diffraction spectrometry pattern was measured using Shimadzu XRD-6100 diffractometer (Cu K a radiation). Steady-state photoluminescence (PL) and time-resolved PL decay were conducted by time-resolved luminescence decays with time-correlated single photo counting system (Pico Harp 300, Pico Quant GmbH). A laser beam with an excitation

wavelength of 532 nm was used to excite the perovskite layer from the air side. The photocurrent density-voltage (J-V) characteristics of PSCs were measured under 1 sun illumination using a programmable Keithley 2400 digital source meter with AM 1.5 G simulated solar light. The external quantum efficiency (EQE) measurement was obtained under alternating current (AC) model (130 Hz). The electronic impedance spectra (EIS) characteristics were recorded the Autolab PGSTAT 30 (Eco Chemie B.V., Utrecht, The Netherlands) and the frequency range from 0.01 Hz to 1 MHz with oscillating amplitude of 10 mV. The Z-view software (v2.8 b, Scribner Associates Inc.) was used to analyze the impedance spectra.

Computational Details

Our calculations were carried out by using the Vienna ab initio simulation package (VASP)[3] based on density functional theory (DFT) method. The generalized gradient approximation potential[4] of Perdew–Burke–Ernzerh of was used to deal with the electron exchange-correlation interactions. The plane-wave cutoff energy was set to 400 eV for all the computations. The Brillouin zone was sampled using the $3\times3\times1$ gamma-centered k-points grids for structure relaxations and energy calculations. To prevent artificial interactions between periodic images, a vacuum space of 20 Å was applied in the z-direction (perpendicular to the surface. The convergence tolerance for the residual force on each atom during structural relaxation was set to 0.01 eV/Å, and the energy difference between two consecutive self-consistent calculations is less than 10^{-4} eV. To describe the weak interactions between the $CsPbI_3$ and Mo doped SnO_2 nanosheets, we performed an empirical correction by using the DFT-D_3 method in Grimme's scheme.[5]

Table S1 A brief summary of the morphology and the crystallization controls of the inorganic CsPbI$_3$ perovskite film based on different underlayers using different strategies.

| underlayers	Strategies	Cell configuration	V_{oc} (V)	J_{sc} (mA/cm^2)	FF	PCE (%)	Ref.
High-temperatur TiO$_2$	choline iodine (CHI) surface treating	FTO/c-TiO$_2$/perovskite/CHI/ spiro-OMeTAD/Ag	1.11	20.23	82.00	18.40	*Science*, **2019**, 365,591–595
	phenyltrimethylammoniu m chloride (PTACl) surface treating	FTO/c-TiO$_2$/perovskite/PTACl/ spiro-OMeTAD/Ag	1.137	20.23	82.70	19.03	*Angew.Chem.Int.Ed.* **2019**, 58,16691 – 16696
	volatile additive (DMAI)	FTO/c-TiO$_2$/perovskite- DMAI/ spiro-OMeTAD/Ag	1.066	20.09	77.60	16.62	*Angew.Chem.Int.Ed.* **2019**, 58,16691 – 16696
	quaternary ammonium salt (TBAI) surface treating	FTO/c-TiO$_2$/perovskite/ TBAI/ spiro-OMeTAD/Ag	-	-	-	18.32	*Angew. Chem.* **2021**, 133, 1 – 6
	phenylethylamine iodide (PEAI) surface treating	FTO/c-TiO$_2$/perovskite/ PEAI/ Spiro-OMeTAD/Ag	1.09	-	79.00	17.08	*J.Energy.Chem*, **2020**.*48* , *181–186*
	Adamantanemethylamin e (ADMA) additive	FTO/TiO$_2$/CsPbI$_3$- ADMA/ Spiro-OMeTAD/Au.	1.09	18.29	80.50	16.04	*Adv. Energy Mater.* **2020**, *10*, 1903751
	urea-ammonium thiocyanate (UAT) molten salt additive	FTO/TiO$_2$/CsPbI$_3$- UAT/ Spiro-OMeTAD/Au.	1.148	20.76	84.30	20.08	*Angew.Chem. Int.Ed.* **2021**, *60,13436 –13443*
	methylammonium chloride (MACl) surface treating	FTO/TiO$_2$/CsPbI$_3$/ MACl/ Spiro-OMeTAD/Au.	1.198	20.59	82.50	20.37	*Joule*, **2021**, *5 ,183-196.*
Low-temperatur SnO$_2$	Zn(C$_6$F$_5$)$_2$ Additive	FTO/SnO$_2$/CsPbI$_3$- Zn(C$_6$F$_5$)$_2$/ Spiro-OMeTAD/Au.	1.12	20.67	81.98	19.00	*Adv. Mater.* **2020**, 2001243
	phenylethylammonium (PEA) additive	ITO/SnO$_2$/LiF/PEA-CsPbI$_3$/ SpiroOMeTAD/Au	1.32	17.74	72.50	17.00	*Small*, **2020**, *16*, 2005246
	2-phenylethanamine iodide(PEAI) additive	ITO/SnO$_2$/PEA$_2$Cs$_{n-1}$PbnI$_{3n+1}$/SpiroOMeTAD/Au	1.07	16.59	70.00	12.40	*Joule*, 2018, 2, 1.
	DMF and DMSO solvent-controlled growth (SCG)	ITO/SnO$_2$/CsPbI$_3$/Spiro-OMeTAD/Au	1.08	18.41	79.32	15.70	*Nat. Commun*, **2018**, 9, 2225.
	dual-passivation ligands amino acids（AA）surface treating	ITO/SnO$_2$/CsPbI$_3$ QDs/Spiro-OMeTAD/Ag	1.22	17.66	63.00	13.66	*ACS Nano*, **2019**, 13, 11988–11995.
	tert-butyl iodide (TBI) and nucleophile trioctylphosphine (TOP) surface treating	ITO/SnO$_2$/CsPbI$_3$ QDs/Spiro-OMeTAD/Ag	1.27	17.71	72.00	16.21	*Energy Environ. Sci.*, **2021**, 14, 4599
	Mo-SnO$_2$ acts as seed-like sites of CsPbI$_3$ crystal	ITO/Mo-SnO$_2$/CsPbI$_3$/ Spiro-OMeTAD/Au.	1.11	19.69	79.62	17.41	This work
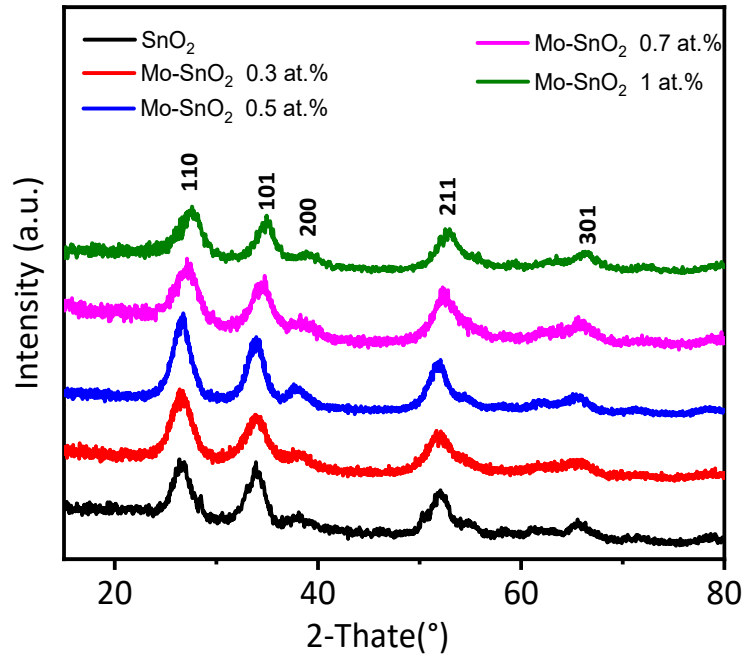
Fig. S1 XRD pattern of SnO_2 films with variable variable Mo doping concentrations (0-1at.%).

Table S2 Diffraction angle (°C), Full width at half maximum, and Grain diameter (nm) of the (110) diffraction peak of Mo-SnO$_2$ NCs using Debye-Scherrer formula simulation.

	110 (0 at.%)	110 (0.3 at.%)	110 (0.5 at.%)	110 (0.7 at.%)	110 (1 at.%)
2θ(°C)	26.6	26.6	26.6	27.2	27.8
FWHM	2.341	2.247	2.185	3.093	3.314
D(nm)	3.643	3.796	3.905	2.761	2.577

The simulation of the (110) diffraction peak of SnO$_2$ NCs with Debye–Scherrer formula reveals a slightly reductive nanocrystals size upon introducing more Mo atoms, which may be ascribed to the suppression of the formation of long-range order caused by the introduction of excessive heterogeneous Mo atoms within the host lattice.
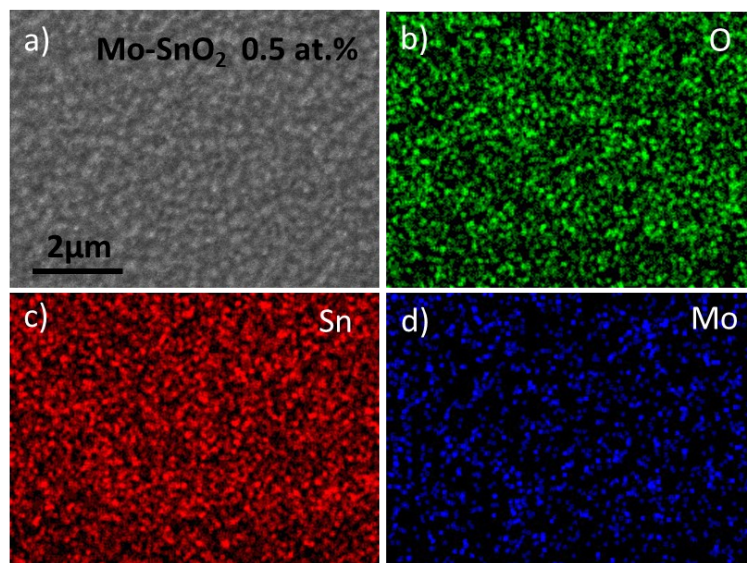
Fig. S2 a) SEM morphology of Mo-SnO$_2$ film with 0.5 at.% Mo doping, and EDS mapping images of Mo-SnO$_2$ film with 0.5 at.% Mo doping for elements: b) O, c) Sn and d) Mo.
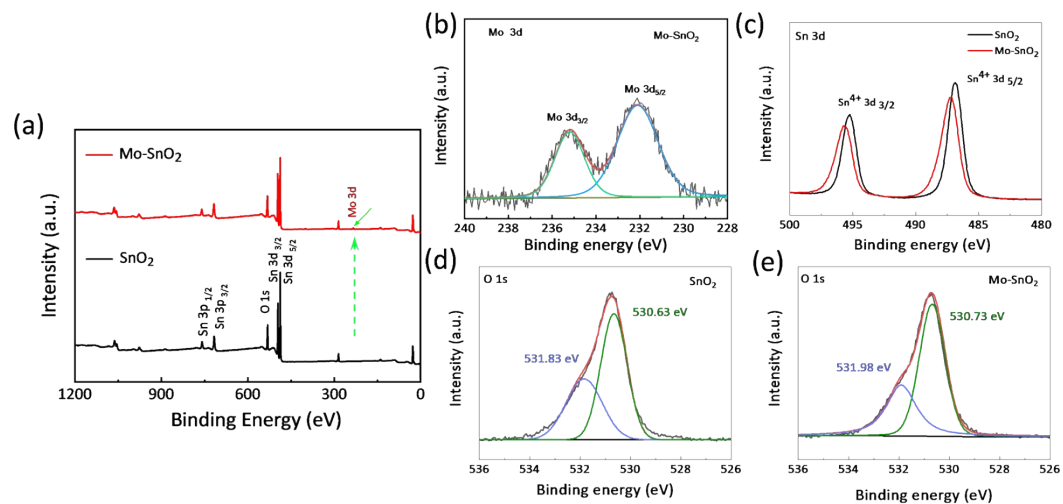
Fig. S3 X-ray photoelectron spectroscopy of Mo-SnO$_2$ and pure SnO$_2$ ETL for (a) full spectrum and (b) Sn 3dpeaks. (c) Mo 3d peaks for Mo-SnO$_2$ ETL , (d) and (e) are O 1s peaks of pure SnO$_2$ and Mo-SnO$_2$ ETL layers, respectively.
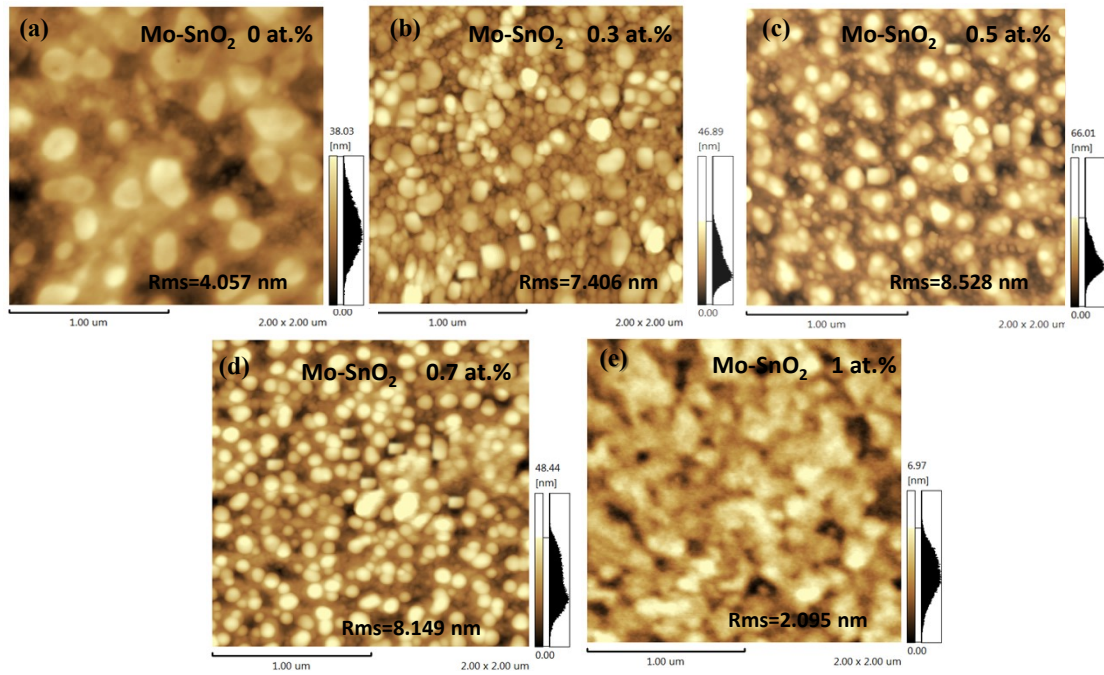
Fig. S4 AFM images (size: 2×2 μm) of Mo-SnO$_2$ with varied Mo doping ratio. a) 0, b) 0.3 at.%, c) 0.5 at.%, d) 0.7 at %, and e) 1 at.% on ITO substrate. Rms is the root-mean-square roughness values can be estimated from Nano-Scope Analysis software.
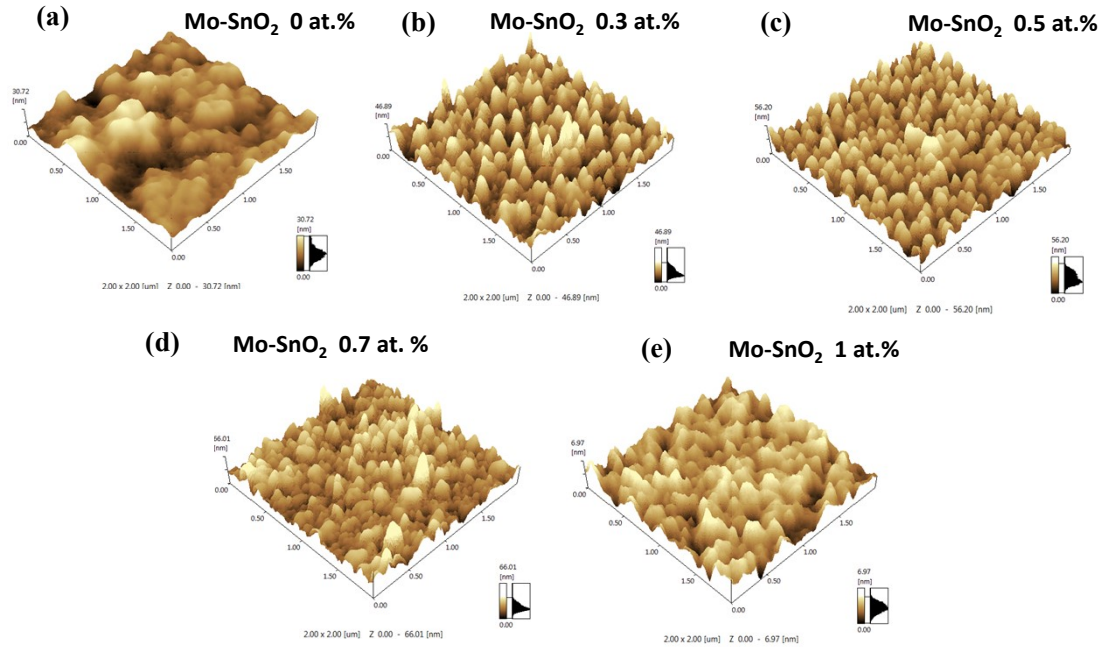
Fig. S5 AFM height images (size: 2×2 μm) of the surface morphology of Mo-SnO$_2$ with varied Mo doping ratio. a) 0, b) 0.3 at.%, c) 0.5 at.%, d) 0.7 at %, and e) 1 at.% on ITO substrate.
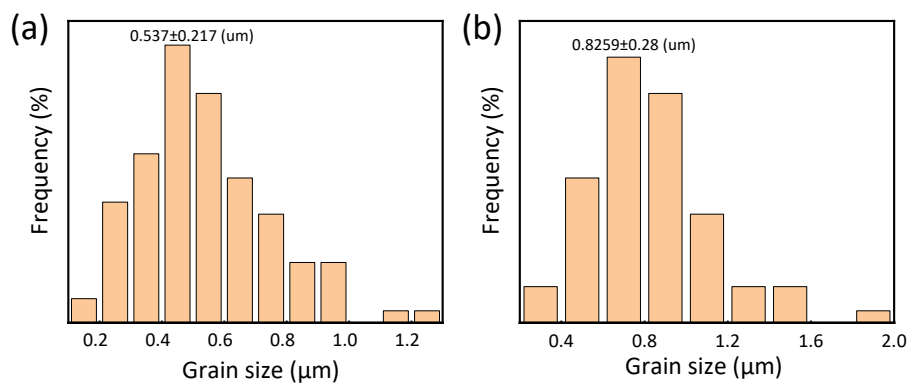
Fig. S6 Granularity statistics of perovskite grain in perovskite thin films deposited on SnO_2 and Mo-SnO_2 ETLs coming from Figure 2f and 2h, respectively.
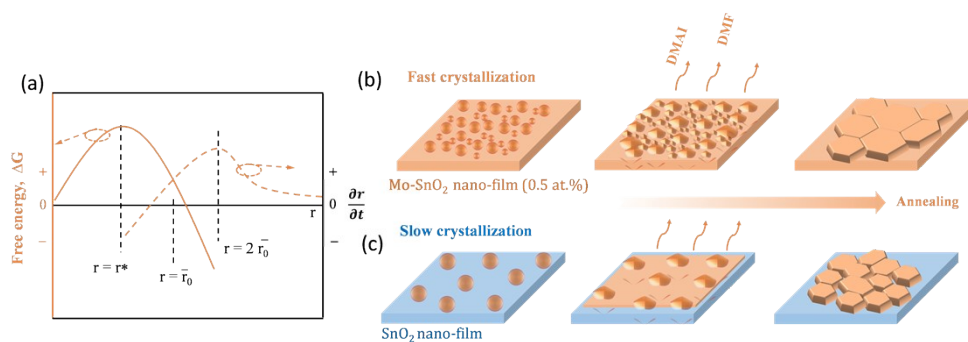
Fig. S6 a) The relationship between Gibbs free energy and particle growth rate and particle radius, respectively. r∗, critical nucleus radius; $\bar{r}_o$, average particle radius. b) Illustration of the difference of slow and fast of nucleation and growth process and their effects on the final film after thermal annealing.

According to classical nucleation theory, when the particle radius (r) is smaller than the critical crystal nucleus r∗ (i.e., r＜r∗), it will be dissolved and disappear and unable to form a stable nucleus. Only in r＞r∗ can particle exist stably and continue to grow, i.e., the probability of continuing to grow is greater than that of disappearing with the solvent, as illustrated in solid yellow line (Figure S6a). Subsequently, drying and thermal annealing processes drive the dissolution and interdiffusion of the of numerous granules inlaying mutually, which forms and grows the large grains. Herein, the granule with the radius r ＜the average particle radius $\bar{r}_o$ cannot grow by themselves, but assist the growth of large particles through spontaneous dissolution and diffusion, as depicted in dashed yellow lines (Figure S6a).
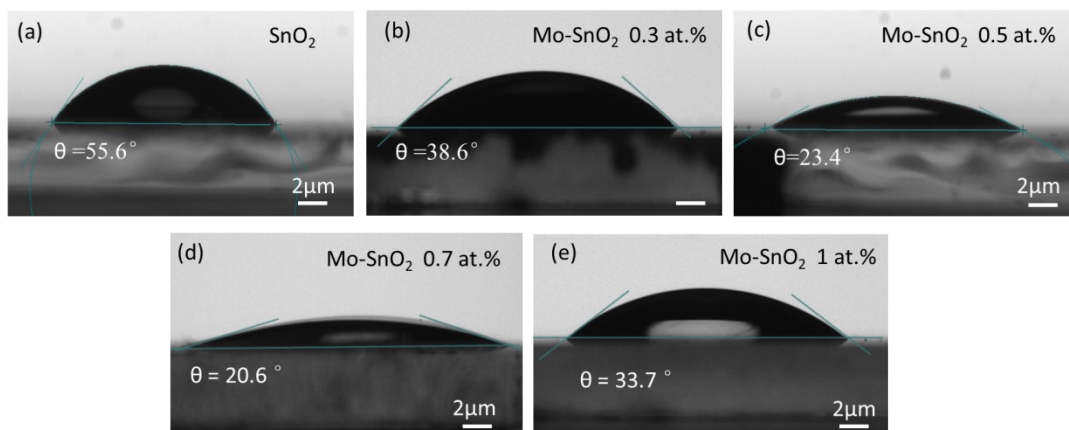
Fig. S7 Contact angle for water on Mo-SnO$_2$ ETLs with various Mo doping concentrations (0-1 at.%)

Surface roughness and surface free energy are the two main factors that dominate the surface wettability. As shown in Figure S7, compared with the pristine SnO$_2$ film, for moderate Mo doping ratios, at 0.5 at.% and 0.7 at.%. For example, in this study the films exhibited obvious decrease of water contact angle. This can be correlated with the fact that the surface roughness occurs under moderate Mo doping of SnO$_2$ and the total amount of surface oxygen vacancies increases.[6-8] Thus Mo doping in SnO$_2$ is effective in boosting the hydrophilicity of SnO$_2$ film. A high ratio of Mo doping refines the crystal grains of SnO$_2$, resulting in a flat surface and a slight increase in roughness.
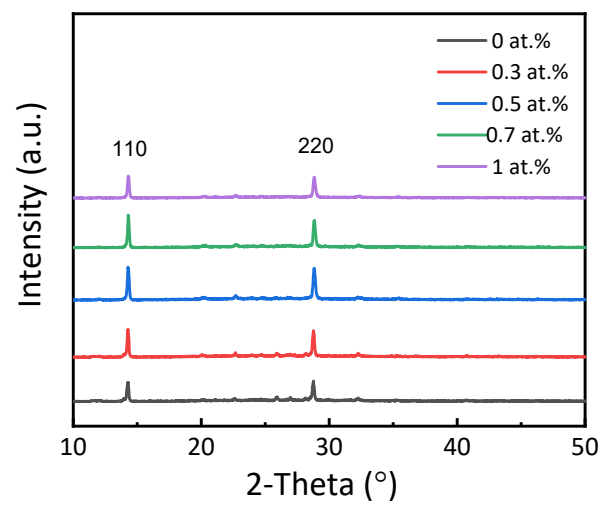
.

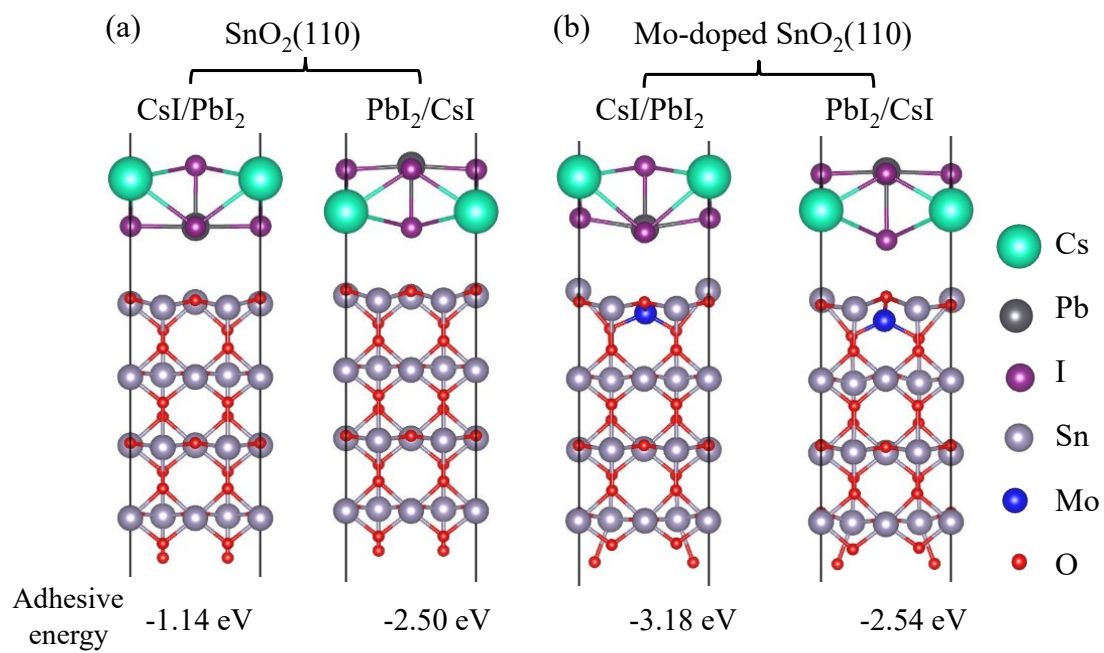**Fig. S9** XRD pattern of perovskite film based on different ETLs.

Fig. S10 Side view of the simplified heterostructure of ETLs and perovskite, optimized geometrical structures and adhesive energies for CsI /PbI$_2$ and PbI$_2$ /CsI adhesion on SnO$_2$ substrates (a) and Mo-SnO$_2$ nucleation sites (b).
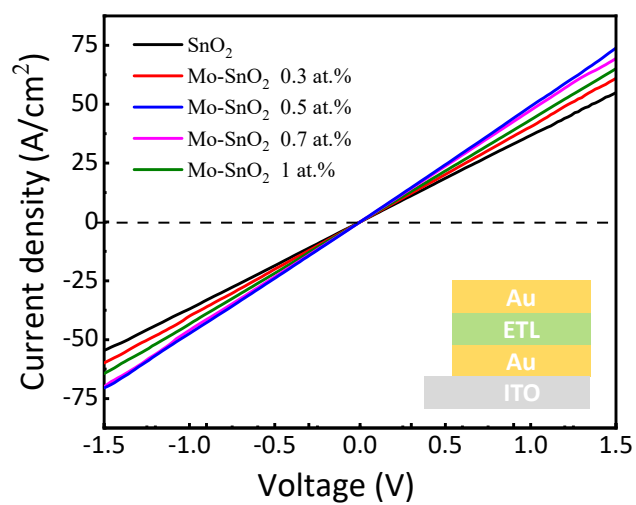
Fig. S11 I-V characteristics of Au/Mo-SnO$_2$/Au with variable Mo doping concentrations (0-1 at.%).

Table S3 Electrical conductivity (σ) of $Au/Mo-SnO_2/Au$ with variable doping concentrations (0-1 at.%).

Sample	Au/ETLs/Au (σ/mS cm^{-1}×10^{-3})
SnO_2	6.23
Mo- SnO_2 (0.3 at.%)	7.52
Mo- SnO_2 (0.5 at.%)	9.04
Mo- SnO_2 (0.7 at.%)	8.62
Mo- SnO_2 (1 at.%)	8.14
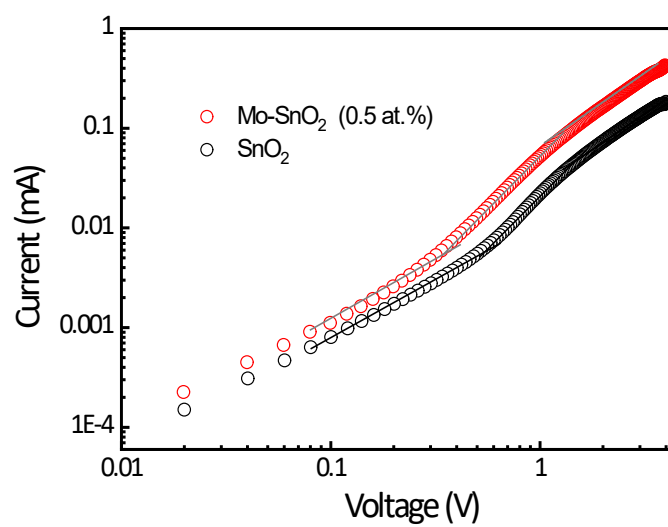
Fig. S12 Dark J-V curves of PSCs based on SnO_2 and Mo^5-SnO_2 ETLs based

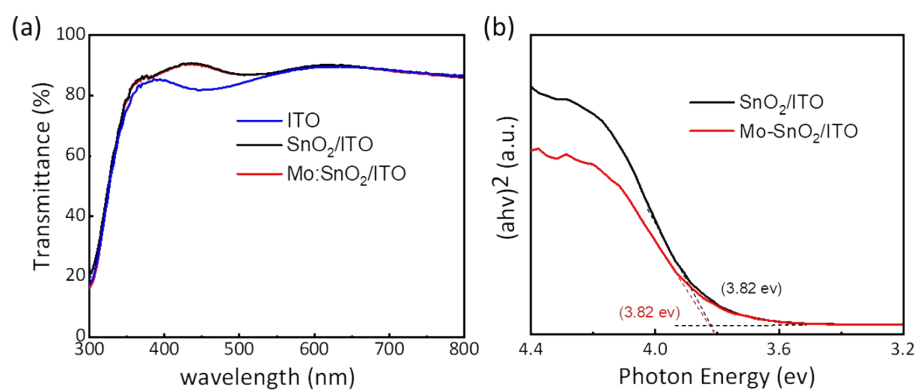electron-dominated devices (ITO/SnO_2/perovskite/$PC_{61}BM$/Ag)

Fig. S13 (a) Transmission spectra of bare ITO, SnO_2/ITO, and Mo-SnO_2/ITO films. (b) The $(ahv)^2$ versus hv plots of SnO_2/ITO and Mo-SnO_2/ITO thin films corresponding to (a).
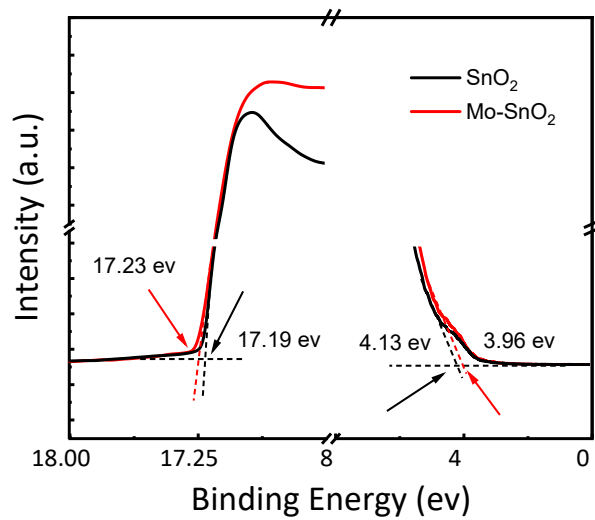
Fig. S14 UPS spectra describing the cutoff energy (E_{cutoff}) and fermi edge (E_F, edge) for SnO_2 and Mo-SnO_2, respectively.
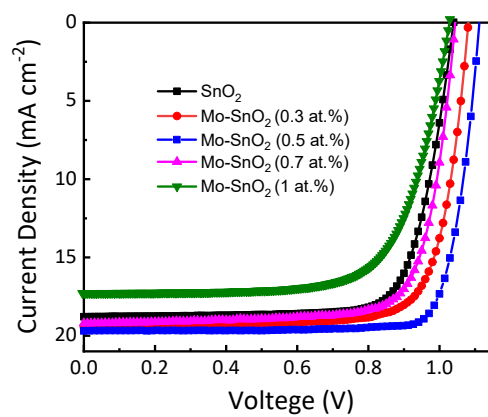
Fig. S15 J-V curves of PSCs based on Mo-SnO$_2$ ETL with various Mo doping concentrations (0-1 at.%)

Table S4 Performance parameters of perovskite solar cell based on Mo-SnO$_2$ with various Mo doping concentrations (0-1 at.%) under illumination of AM 1.5 G, 100 mW cm^{-2}.

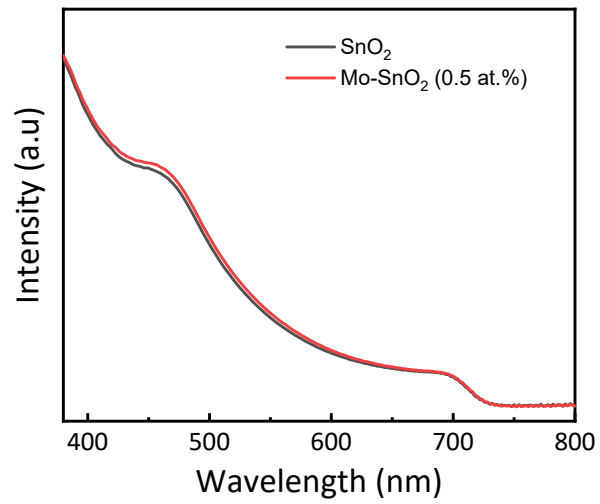| Device	J$_{sc}$ (mA/cm^2)	V$_{oc}$ (V)	FF (%)	PCE (%)
SnO$_2$	18.85	1.04	76.63	15.02
Mo-SnO$_2$ (0.3 at.%)	19.44	1.08	77.75	16.32
Mo-SnO$_2$ (0.5 at.%)	19.69	1.11	79.62	17.41
Mo-SnO$_2$ (0.7 at.%)	19.19	1.05	76.90	15.49
Mo-SnO$_2$ (1 at.%)	17.27	1.03	71.47	12.71

Fig. S16 Absorption spectra of perovskite films deposited on SnO_2 and Mo-SnO_2 (0.5 at.%) ETLs.

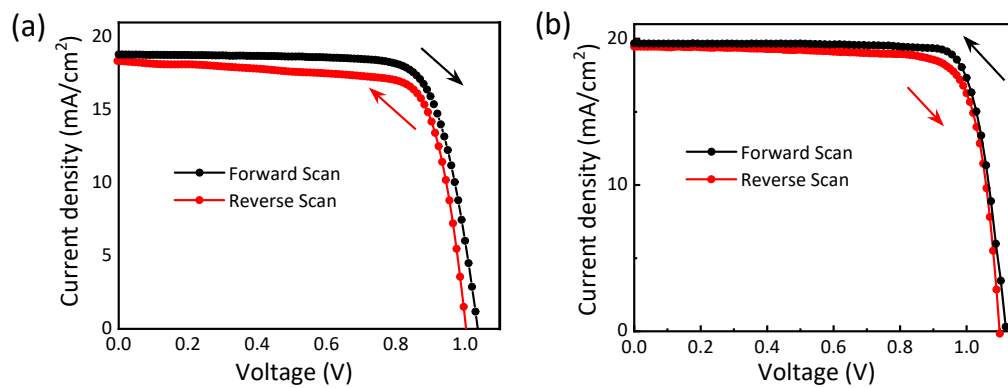**Fig. S17** *J-V* curve of perovskite solar cells based on SnO_2 and $Mo-SnO_2$ (0.5 at.%) measured with reverse (1.2 V→0 V, 0.05V/s) and forward scan (0 V→1.2 V, 0.05V/s), respectively, under AM 1.5G illumination of 100 mW cm^{-2}.

Table S5 Photovoltaic parameters and hysteresis index (HI) of perovskite solar cells based on SnO_2 and Mo-SnO_2 (0.5 at.%) measured with different scan direction with scan rate of 0.05 V/s, Related to Fig. S12.

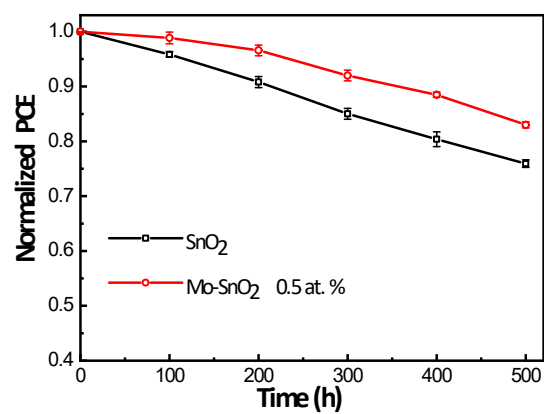| Device	J_{sc} (mA/cm^2)	V_{oc} (V)	FF (%)	PCE (%)	HI
Ref-reverse	18.85	1.04	76.63	15.02	
Ref-forward	18.13	1.00	74.82	13.56	0.054
0.5 at.% Mo-SnO$_2$ reverse	19.69	1.11	79.62	17.41	
0.5 at.% Mo-SnO$_2$ forward	19.52	1.09	78.20	16.62	0.015

Fig. S18 Stability of f PSCs based on SnO_2 and Mo-SnO_2 ETL measured under one sun illumination. Simple encapsulated devices are tested in the air with humidity of 50% -60% .

References

1 Chen, D. Ge, J. Zhang, R. Chu, J. Zheng, C. Wu, Y. Zeng, Y. Zhang, H. Guo, *Nanosca*le, 2018, **10**, 17378-17387.

2 Y. Bai, Y. Fang, Y. Deng, Q. Wang, J. Zhao, X. Zheng, Y. Zhang, J. Huang, *ChemSusChem*, 2016, **9**, 2686-2691.

3 G. Kresse, J. Furthmüller, *Physica B.*, 1996, **54**, 11169-11186.

4 J. P. Perdew, K. Burke, M. Ernzerhof, *Phys Rev. Lett.*, 1996, **77**, 3865.

5 S. Grimme, J. Antony, S. Ehrlich, H. Krieg, *J. Chem. Phys*., 2010, 1**32**, 154104.

6 D. Dhar Purkayastha, M. Krishna, M. Vinjanampati, Mater. Lett., 2014, 124, 21-23.

7 A. Chen, X. Peng, K. Koczkur, B. Miller, *Chem. Commun. (Camb).*, 2004, 17, 1964-1965.

8 W. Zhu, X. Feng, L. Feng, L. Jiang, *Chem. Commun. (Camb).*, 2006, 26, 2753-2755.